# Break-off Model for $CaCO_3$ Fouling in Heat Exchangers

Ivo Babuška

*Institute for Computational Engineering and Sciences The University of Texas at Austin - USA*

Renato S. Silva*

*Laboratório Nacional de Computação Científica - MCTI - Brazil*

Jonas Actor*

*Department of Computational and Applied Mathematics, Rice University - USA*

**Abstract**

*Keywords:* Heat Exchanger, Crystallization Fouling, $CaCO_3$.

## 1. Introduction

Fouling in industrial heat exchangers is a complex, serious problem that occurs when a fouling substance builds along the walls of a heat exchanger, limiting the efficiency of the heat transfer within the system. This has significant impact on the performance of the equipment, increasing projected overhead and maintenance costs [1, 2, 3, 4, 5]. The complexity of fouling is outlined by Epstein in [6], which identifies five mechanisms that occur in the fouling process: initiation, transport, attachment, removal, and aging.

In an effort to understand the fouling process and to quantify its effects, several models have been presented in previous literature [1, 5, 7, 8, 9]. Each of these models develops upon previous work by incorporating new, more detailed explanations of the individual mechanisms at play. Currently, the best proposed models include terms for deposition, transport, and attachment in addition to several mechanisms to explain mass removal.

*Corresponding author
*Email address:* rssr@lncc.br (Renato S. Silva)

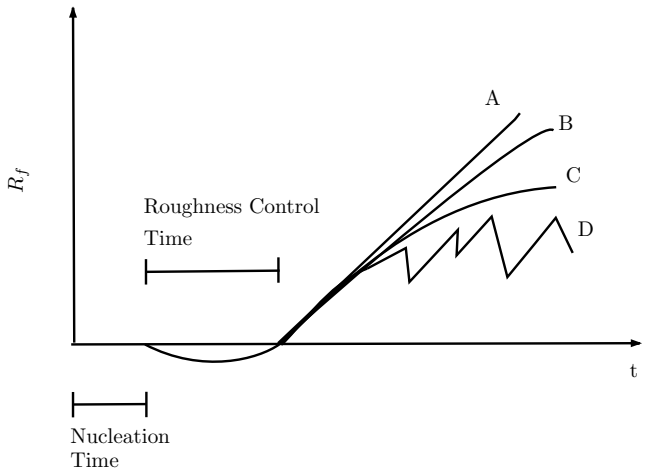


Figure 1: Curves of standard fouling models

In general, the behavior of an ideal model [6, 1, 5] can be characterized by a curve describing the thermal efficiency of the system. These curves take a few distinct forms, as seen in Fig.1. A linear fouling curve (Fig.1-A) is obtained when the removal rate is negligible in relation to the deposition rate, or it is constant but lower than the deposition rate, i.e. when the net deposition rate is constant. A falling rate curve (Fig.1-B) occurs when the rate of deposition falls over time, or the removal rate increases over time, causing the overall net fouling rate to fall. Asymptotic rate behavior (Fig.1-C) is observed for deposits where the removal rate and deposition rate eventually equalize, causing the net fouling rate to approach zero.

However, these curves are all idealized behavior. In experimental results and industrial data, there are distinct oscillations in the thermal efficiency curves (Fig.2). A more realistic thermal efficiency curve is the saw-tooth curve (Fig.1-D), which maintains an overall asymptotic behavior but is marked by the removal of a large amount of material at certain distinct times. Such behavior was mentioned in literature as early as the first models proposed by Kern and Seaton [9], and according to Epstein this is not an unusual behavior [10].

Unfortunately, fouling thickness is not directly measurable during experi-

mentation. Instead, the quantity of interest is a time-dependent measure of thermal resistance. Figure 2 shows some typical recordings of thermal resistance from experimental data. It is clear that the apparent randomness in the data cannot be explained by instrumentation or measurement error alone. We anticipate that there is a random process to describe the breaking of portions of the fouling deposit. This paper proposes a model for $CaCO_3$ crystalline fouling in heat exchangers that incorproates a mass reomval rate based on breaking due to thermal stress compared to the strength of the fouling material, varying with age.

We construct our enhanced breaking model in relation to work from two previous studies. The first, by Yiantsios et. al. [11], adopts a population model to characterize discrete breaks. They consider only shear stress and a log-normal distribution to describe the critical stress required for breaking. The second is the work of Brahim et. al. [12], which is an extension of the Bohnet model [13]; this model defines the fouling density as a function of the size of the fouling layer, which in turn depends on the age of the layer itself. Doing so allows for age to play a role in layer strength, and also allows for the thermal resistance to change with age, in a more realistic manner.

The aim of this paper is to propose a new model that is capable of reproducing the breaks in the fouling layer encountered in experimental results, making two significant improvements over previous work. First, we enhance the removal term so that it considers aging. This allows us to evaluate the temperature distribution in each layer, permitting us to include the effects of thermal stress, which dictates when pieces of the fouling layer break. Second, we consider the polymorphism that $CaCO_3$ crystals take. The change in crystal structure effects basic material properties, such as the strength and thermal conductivity. We do this using a probability distribution to describe the diameter of the crystal that forms at each layer of the fouling layer, at each point in the pipe. We calibrate our model and measure its accuracy via least-squares error and Akaike Information Criterion in relation to the Kern and Seaton model. Unfortunately, there are not many sources for industrial or experimental data, and due to the

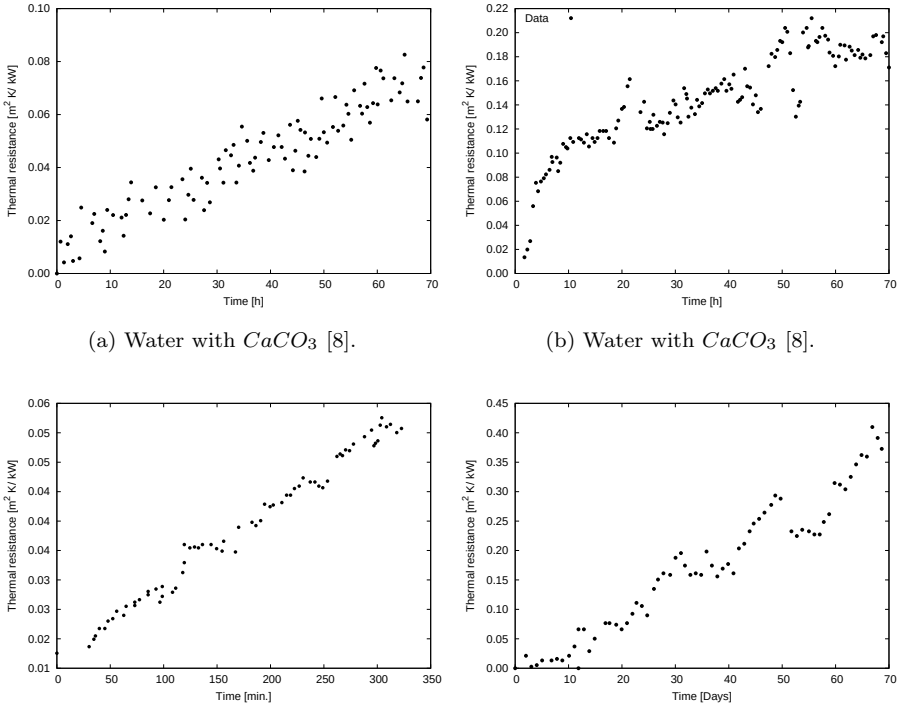


(a) Water with $CaCO_3$ [8].

(b) Water with $CaCO_3$ [8].

(c) Water with $CaCO_3$ [14].

(d) Sea water, biofouling [15].

Figure 2: Experimental data from fouling literature.

lack of experimental results, we focus on the calibration of our model for the data we did obtain. We will compare our results to other models in future work.

The outline of the paper is as follows. Section 2 describes our breaking model, which is then analyzed and discussed in Section 3. We then proceed to describe the Kern and Seaton model in section 4, before proceeding in Section 5 to briefly introduce the data used and the numerical methods adopted. At this point, we present our results. Finally, Section 6 presents the final conclusions and suggests directions for future research.

## 2. Break-off model

Figure 2 displays examples from literature of recorded measurements of thermal resistance in heat exchanger that exhibit fouling. It is obvious this phenomenon is subject to large fluctuations due to differences in fouling. We wish to capture the behavior underlying this system. However, there is not enough available data, nor are there cases of experimental repetition using the same parameters. We have for consideration only single observations in two different regimes of cooling, from [8]. Because of this, we concentrate on the calibration phase of the modeling.

The Break-off (BO) model has three parts:

- The general heat transfer model;
- The model of the fouling growth;
- The thermal resistance.

See the notation section for symbols definitions and their dependencies.

### *2.1. The heat transfer problem*

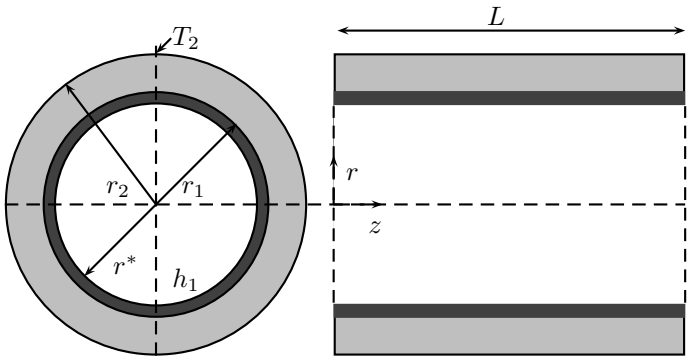


Figure 3: The geometry of the pipe (gray) with fouling layer (dark gray)

The heat transfer problem operates under the assumption that the fouling thickness $\delta$, the physical properties of the fouling layer, and the properties of

water are known. The temperature distribution in the pipe and in layer is determined by

$$-\frac{1}{r}\frac{\partial}{\partial r}\left(rk(T_1(r,z,t))\frac{\partial T_1(r,z,t)}{\partial r}\right)=0, \tag{1}$$

where

$$r^*(T,z,t)\le r\le r_2,\ 0\le z\le L,\ 0\le t\le \hat{t} \tag{2}$$

with boundary conditions:

$$-k(T_1(r^*,z,t))\frac{\partial T_1(r^*,z,t)}{\partial r}+h_1(T_1(r^*,z,t),T(z,t))(T_1(r^*,z,t)-T(z,t))=0 \tag{3}$$

where $r^*(z,t)$ is the radius of the pipe with fouling and $T_1(r_2,z,t)=T_2$.

The thermal conductivity is defined as

$$k(T_1(r,z,t))=\begin{cases}k_s(T_1(r,z,t)), & \text{for } r_1\le r\le r_2;\\ k_f(T_1(r,z,t)), & \text{for } r^*(z,t)\le r\le r_1.\end{cases} \tag{4}$$

For the convection coefficient $h_1$ we used

$$h_1(T)=\frac{k_w(T)}{2r_1}\frac{\left(Re(T)Pr(T)\left(\frac{f}{2}\right)\right)}{1+\sqrt{\frac{f}{2}}\left[4.5Re_\epsilon(T)^{0.2}Pr(T)^{0.5}-8.48\right]}. \tag{5}$$

proposed by Bhatti and Shah, where $Re_\epsilon$ is the roughness Reynolds number defined as $Re_\epsilon(T)=\epsilon u/\nu(T)$. This correlation is valid for $0.5<Pr<10$, $0.002<\epsilon/r_1<0.05$ and $Re>10^4$ [16].

We used the friction factor proposed by Nikuradze,

$$f=\left(3.48-1.737\ln\left(\frac{\epsilon}{r^*}\right)\right)^{-2}. \tag{6}$$

The temperature of the water inside the pipe satisfies

$$\bar{m}(T(z,t))c_p(T(z,t))\frac{\partial T(z,t)}{\partial z}=Q(z,t), \tag{7}$$

with initial condition $T(0,t)=T_0$ and

$$\bar{m}(T(z,t))=\pi r^{*2}u(z,t)\rho(T(z,t)). \tag{8}$$

Moreover, $Q(z,t)$ is the heat received by the water obtained as:

$$Q(z,t) = -2\pi r^* k_f (T_1(r,z,t)) \frac{dT_1(r,z,t)}{dr}. \tag{9}$$

The velocity at each point is enforced by continuity,

$$u(z,t) = \frac{r^*(z,0)}{r^*(z,t)} u(z,0). \tag{10}$$

This formulation allows us to consider the reduction in section due to the growing of the layer.

### *2.2. The Fouling Model*

The rate of fouling mass growth $m_f(z,t)$ is the difference between the rate of deposited mass $m_d(z,t)$ and the rate of mass removed $m_r(z,t)$, with

$$\frac{dm_f(z,t)}{dt} = \frac{dm_d(z,t)}{dt} - \frac{dm_r(z,t)}{dt} = \dot{m}_d - \dot{m}_r. \tag{11}$$

The rate of deposition mass is the same used in the Bohnet model [13] with transport and attachment phases defined as

$$\begin{aligned} \dot{m}_d = K_d \Bigg\{ & \frac{1}{2}\left(\frac{K_d}{K_r}\right) + (c_F - c_s) - \\ & - \sqrt{\frac{1}{4}\left(\frac{K_d}{K_r}\right)^2 + \left(\frac{K_d}{K_r}\right)(c_F - c_s)} \Bigg\}, \end{aligned} \tag{12}$$

where $K_d$ is the the mass transfer coefficient defined in Eq. 13, and $D$ is the mass diffusion coefficient given in [17],

$$K_d = 0.023 Sc^{0.33} Re^{0.85} D/d_h. \tag{13}$$

The coefficient of surface reaction $K_r$ is given by Arrhenius's law,

$$K_r = K_{r0} \exp\left(-\frac{E}{RT_s}\right). \tag{14}$$

The removal term $\dot{m}_r$ relates to the removal of the recently deposited 'dust' of $CaCO_3$ material, and the breaks that occur in crystals grown previously.

$$\dot{m}_r = \dot{m}_r^d + \dot{m}_r^b. \tag{15}$$

For $\dot{m}_r^d$ we utilize a version of the Bohnet removal term, given as

$$\dot{m}_r^d = C_B \rho_f \left(\rho^2 \mu g\right)^{\frac{1}{3}} \delta u^2 \ . \tag{16}$$

where $C_B$ is a constant defined in the similar way as in [13]. We differ from the Bohnet model in that the thermal stress term and the crystal diameter ($d_p$) are considered separately.

The breaking relates to the thermal stress $\sigma$ by

$$\sigma(r, z, t) = E_y \alpha \Delta T, \tag{17}$$

where $\Delta T = (T_b - T_1(r, z, t))$ and $T_b$ is the temperature of the material at the time it was formed. We assume this temperature is equal to that of the surrounding water for that given time and location. The strength of the material $\bar{S}$ of the material is adapted to depend on the age of the material $S_{age}(r, z, t)$,

$$\bar{S}(r, z, t) = \frac{d_p}{\xi} \left( S_0 + (S_1 - S_0) \left( 1 - \exp\left( \frac{-S_{age}(r, z, t}{\alpha_s} \right) \right) \right), \tag{18}$$

where $\xi$ is a random variable with uniform density probability that explains the changes in crystal size;

$$\xi = U\left[d_p^{[1]}; d_p^{[2]}\right]; \quad 0 < d_p^{[1]} < d_p^{[2]} \tag{19}$$

with $d_p^{[1]} = dp - \sigma_{dp}$ and $d_p^{[2]} = dp + \sigma_{dp}$. This probability allows us to consider which crytal polymorphs of $CaCO_3$ are present at each position in the fouling layer. Breakage occurs if

$$\sigma^* = \max \sigma(r, z, t) = \sigma(r^b, z, t) = \bar{S}(r, z, t); 0 < r^b < r^* \tag{20}$$

so that

$$\dot{m}_r^{[b]} = \begin{cases} 0, & \text{if } \sigma^* < \bar{S}(r, z, t); \\ \rho_f (r^* - r^b), & \text{if } \sigma = \bar{S}(r, z, t). \end{cases} \tag{21}$$

The material transformation described by Eq. 18 also represents the change in the thermal conductivity in the form of

$$k_f = k_{f,0} + (k_{f,1} - k_{f,0}) \left( \exp\left( \frac{-S_{age}(r, z, t)}{\alpha_k} \right) \right), \quad r^1 < r \leq r^*. \tag{22}$$

This expression is utilized in Eq. 4 for determining the thermal conductivity of the fouling layer.

The radius of the pipe with fouling is approximated by

$$r^* = \frac{m_f}{2\pi r_1 \Delta_z \rho_f}. \tag{23}$$

*2.3. Thermal Resistance*

The thermal resistance $R_f(z,t)$ is the standard quantity of interest in the fouling community because it directly relates to the fouling growth. For cylindrical geometries with variable properties, it is defined as

$$R_f(z,t) = \frac{r_1 \ln\left(\dfrac{r_1}{r^*(z,t)}\right)}{k_f(T_1(r,z,t))}. \tag{24}$$

To make it compatible with industrial standards, we use the mean value for thermal conductivity across the length of the pipe, defined as

$$\bar{R}_f(t) = \frac{1}{L}\int_0^L \frac{r_1 \ln\left(\dfrac{r_1}{r^*(z,t)}\right)}{\bar{k}_f} dz \ , \tag{25}$$

where $\bar{k}_f$ is the thermal conductivity obtained at the mean temperature in the fouling section $(T_1(r^*) + T_1(r_1))/2$.

## 3. Analysis of the model

In this section we will address many of the underlying assumptions of the model. In break-off model, we assume the solution is rotationally symmetric; as a result, we interpret the any of the values under consideration as averages over the angle $\theta$, $0 \leq \theta < 2\pi$.

*3.1. Heat transfer model*

The heat transfer model is quasi-stationary, as the uncertainty in material property and the small thickness of the fouling layer allow for use to disregard heat transfer along the $z$ direction along the pipe's primary axis. The comparatively high velocity of the water makes the loss due to this assumption negligible.

Thus, we assume that heat flux only occurs in the $z$ direction in the pipe. We also assume all the properties of water are function of temperature, they are given by the definitions in [18].

We use a hydraulic diameter approximation because we consider averages of fluid temperatures and velocities. This approximation is used elsewhere, and is the same as in [8] in the calculation of the thermal resistance. Therefore, our heat transfer model simplifies to solving for a single pipe with a hydraulic diameter for the annular section and with an external wall temperature equal to the surrounding vapor temperature, as assumed in [8].

The flow inside the pipe is considered turbulent and fully developed.

### *3.2. Fouling model*

The saturation concentration for the $CaCO_3$ is evaluated by the equations given in [19]. We assumpe the $CaCO_3$ concentration is constant in the $z$ direction. Our model induces material changes in thermal conductivity and in material strength to simulate the aging process. Several authors recognize the aging process for the crystallization fouling; many mention [6, 5, 8, 20, 21, 12, 22, 23] that the aging process for the $CaCO_3$ increases the strength of the layer by recrystallization, additional reorientation and/or transformation into a different polymorph [5, 21], thereby altering the thermophysical properties of the layer.

We approximate the aging process by exponential curves (Eqs. 18,22), simulating the relative concentrations of each of the $CaCO_3$ polymorphs vaterite, aragonite, and calcite, described in Figure 4.

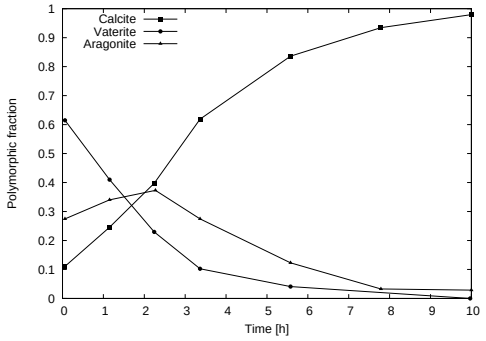


Figure 4: Relative concentrations of $CaCO_3$ polymorphs at 40℃. Adapted from [24]

The random variable $\xi$ represents the different crystal types of the initial deposited material, relating to the initial point ($t = 0$) in Fig. 4. In this way, $\xi$ is a new material property, attributed to the fouling material at the time it is created and held fixed for that position in the fouling layer throughout the simulation.

### *3.3. Thermal Resistance*

Since the thermal conductivity is function of $r$, $z$, and $t$, and the thickness of the fouling layer is also function of $z$, we use a more general definition of thermal resistance that incorporates dependence on these variables.

### *3.4. Numerical Procedure*

The numerical procedure used to simulate the break-off model can be summarized as follows.

- For each $t_j$
  - For each point $z_i$
    1. evaluation of the water temperature:
       - evaluation of the age of the material
       - evaluation of the new $k_f$ and $\bar{S}$ factors (Eqs 22,18)

        * evaluation of the temperature distribution in the layer (Eq. 1)
        * evaluation of the $Q(z_i, t_j)$ (Eq. 9)
        * solve the water temperature (Eq. 7)
    2. evaluation of the *net* material deposited (Eq. 11)
    3. evaluation of the thermal stress (Eq. 17)
    4. evaluation the breaks based on the random sample and update the size of the layer (Eq. 21)
    5. evaluate the new $r^*$ and velocities (Eq. 10,23)
  - increment $z_{i+1} = z_i + \Delta_z$
- evaluate the thermal resistance (Eq. 25)
- increment $t_{i+1} = t_i + \Delta_t$

The evaluation of the water temperature (Eq. 7) is done by dividing the $z$ direction into $n_z$ equispaced points, with spacing of $\Delta_z$, and then applying the first order Adam's method [25](Sec. III-1). However, it is necessary to evaluate $Q_i$, along with the temperatures of the newly-deposited fouling material, of previously deposited fouling layers, and of the pipe itself. Temperature is evaluated at each $z_i$ by posing nonlinear problem, where the nonlinearity is due to the convection coefficient at the fouling interface. We solve this problem using an iterative solver with a one dimensional finite element method on a nonuniform mesh, where each element size is set equal to the thickness of each layer of material deposition, adapting to accommodate the sections of the fouling layer that break away. Each element has a uniform $k_f(t)$ and a constant $\xi_i$, assigned when that layer of fouling material is first deposited,

The first order Adam's method is also used for timestepping, with a time step of $\Delta_t = 7.5$ min.

## 4. The Kern and Seaton model

This model (KS) was first introduced by Kern and Seaton [9], and consists of two parts: a model describing the fouling process and a model of the thermal

resistance. It fails to include a specific heat transfer model, and it uses a constant deposition rate independent of temperature. Thus, the properties $\rho_f$ and $k_f$ are fixed.

### *4.1. Fouling Model*

The fouling model included in KS is defined as:

$$\frac{dm_f^{KS}(z,t)}{dt} = \dot{m}_d^{KS} - \dot{m}_r^{KS}. \tag{26}$$

Deposition occurs at a constant rate proportional to the velocity and $CaCO_3$ concentration [9, 1], which is defined as:

$$\dot{m}_d^{KS} = K_1 u c_F. \tag{27}$$

The removal term is an average rate of removal, in that it does not depend on location within the pipe. The main cause of this removal is breaking due to shear stress from the fluid, which is proportional to the thickness of the layer. With these assumptions, the removal term is given by:

$$\dot{m}_r^{KS} = K_2 \tau \delta. \tag{28}$$

Notice that $K_1$ and $K_2$ are constants that we will calibrate to match given data.

### *4.2. Thermal Resistance*

As this model does not have a spatial dimension and the material properties are not dependent on temperature, we utilize the standard definition for fouling thermal resistance [5, 13]. In this case, there are two common assumptions- that the convection coefficients for a clean pipe and for a pipe with fouling are the same, and that the thickness of the fouling layer is small enough so that the thermal resistance for the fouling in a pipe is approximated by

$$R_f(t) = \frac{\delta}{k_f}. \tag{29}$$

*4.3. Numerical Procedure*

For the KS model we utilize the first order Adam's method in time with $\Delta_t = 7.5$ min. The numerical procedure is:

- For each $t_i$

    1. evaluation of the material deposited (Eq. 27)
    2. evaluation of the material removal (Eq. 28)
    3. evaluation of the *net* material deposited (Eq. 26)
    4. evaluate the new $r^*$ and velocities (Eq. 10,23)
    5. evaluate the thermal resistance (Eq. 29)

- increment $t_{i+1} = t_i + \Delta_t$

## 5. Numerical Results

We use experimental data of [8] (see also section 3.1) for Run 23 and Run 20 with experimental parameters given in Table 1.

| | Flow rate $[m^3/s]$ | u $[m/s]$ | Hardness $[mg\ \mathrm{CaCO_3}/l]$ | $T_b$ [℃] | $T_w$ [℃] | $q$ $[kW]$ |
|---|---|---|---|---|---|---|
| Run 20 | 55.00 | 0.695 | 700 | 27.00 | 95.36 | 11.9 |
| Run 23 | 39.83 | 0.503 | 644 | 27.92 | 109.02 | 11.2 |

Table 1: Sheikholeslami's experimental parameters, adapted from [8]

The $R_f$ values from these experiments are shown in Fig. 5

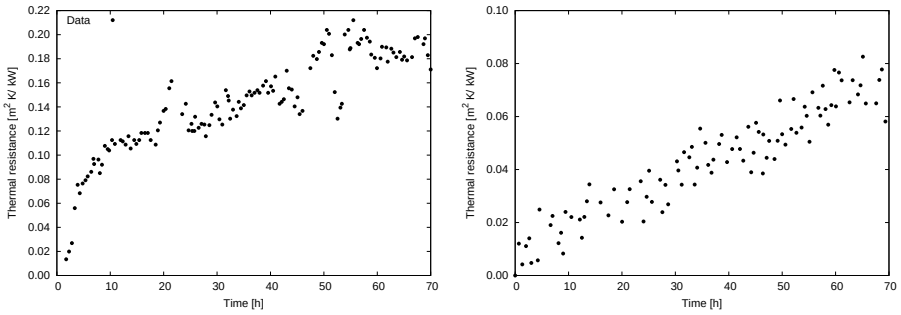


(a) Run 23. (b) Run 20.

Figure 5: Sheikholeslami's Experimental Data for Run 23 and Run 20, adapted from [8].

We see in Fig. 5 a significant difference between these two runs, suggesting fundamental differences in the fouling layer characteristics. In Run 23 we see larger breaks, while in Run 20 breaks occur more frequently and are therefore smaller in magnitude.

Before calibrating both of the models to this data, we select the basic parameters that are more significant to the model by using a sensitivity analysis, described below.

### *5.1. Sensitivity Analysis*

The parameters of the BO model are listed in Table A.1. We use the Elementary Effects method described by Morris [26], which is a global sensitivity method that generates $r_{EE}$ trajectories and then covering the parameter space to evaluate the elementary effects due to the variation. The elementary effect for the $i^{th}$ parameter is defined as

$$EE_i = \frac{f(x_1, x_2, \ldots, x_{i-1}, x_i + \Delta, \ldots, x_k) - f(x_1, \ldots, x_k)}{\Delta}, \tag{30}$$

where $\Delta$ is the increment, given by $\Delta = p/(2(p-1))$, with $p$ being the number of levels into which parameter space is discretized. The sensitivity measures proposed by Morris are the mean (Eq. 31) and the standard deviation

(Eq. 32) of the distribution of the elementary effects obtained using a defined number of trajectories. Another measure commonly used is $\mu^*$ which is defined in Eq. 33 [26], which is the absolute average of the elementary effects.

$$\mu_{EE} = \frac{1}{r}\sum_{j=1}^{r} EE_i^j \tag{31}$$

$$\sigma_{EE} = \frac{1}{r-1}\sum_{j=1}^{r}\left(EE_i^j - \mu_i\right)^2 \tag{32}$$

$$\mu^*_{EE} = \frac{1}{r}\sum_{j=1}^{r}|EE_i^j| \tag{33}$$

Elementary effect scores given by Eq. 31 and Eq. 33, using the conditions from Run 23 for $p = 4$ and $\Delta = 2/3$, are presented in Figure 6. These scores are used to distinguish between three categories of parameters. The first group admits a negligible amount of uncertainty within the model. Groups 2 and 3 are shown via elementary effects to be sensitive enough to need calibration. The parameters with the greatest sensitivities are labeled as group 3. For both scores, we see that group 3 contains the variables $c_f$, $S_0$, $S_1$, $S_{age}$ and $d_p$. These are the ones we will focus on during the calibrations stage of our model analysis.

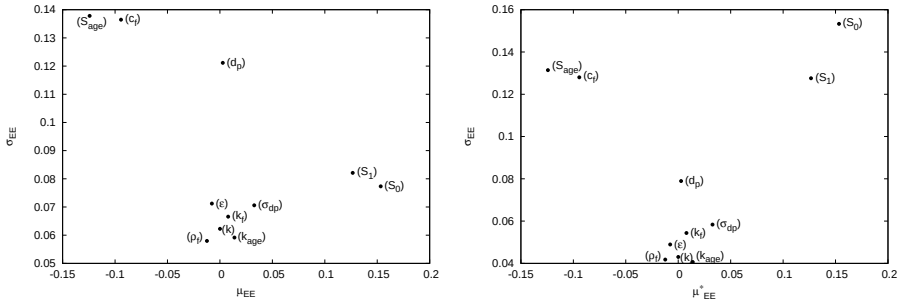


(a) Using $\mu_{EE}$

(b) Using $\mu^*_{EE}$

Figure 6: Estimated parameters $\mu_{EE}$, $\mu^*_{EE}$ and $\sigma_{EE}$ of Morris Elementary Effects with 20 trajectories.

*5.2. Calibration*

Calibration of the BO and KS models was done using a gradient based optimization algorithm to minimize the relative least squares distances, given by

$$ASSq = \sqrt{\frac{1}{N}\sum_{j=1}^{N}(ISSq_j)^2}, \tag{34}$$

where

$$ISSq_j = \sqrt{\frac{\sum_i^M (R_{f,j}(t_i) - x_i)^2}{\sum_i^M x_i^2}} \tag{35}$$

and $x_i, i = 1, \ldots, N$ are the observed data for samples $j = 1, \ldots, M$.

The parameters optimized for the BO model are $S_0$, $S_1$, $S_{age}$, and $d_p$. We additionally calibrated $\sigma_{dp}$ due to it is close relationship with the other parameters selected. In the KS model, the parameters $K_1$ and $K_2$ are optimized. As the KS model includes no probabilistic terms, for KS we view $N = 1$ in the above formulas.

The optimal parameters for the BO model are given in Table 2, 3. For completness, we also include the ISSq for the best and worst samples of the selected BO models.

| # | | | | ASSq | ISSq | |
|---|---|---|---|---|---|---|
| | $S_0$ | $S_1$ | $S_{age}$ | | Best | Worst |
| | $d_p$ | $\sigma_{dp}$ | | | | |
| New Model | 0.7222 | 6.50 | 450.0 | 0.0913 | 0.0871 | 0.3500 |
| | $0.30 \times 10^{-4}$ | $2.50 \times 10^{-5}$ | | | | |

Table 2: Run 23: ASSq for the best set of parameters and the ISSq for the best and worst samples.

For the KS model the optimized parameters for Run 23 are $K_1 = 0.6158 \times 10^{-1}$ and $K_2 = 0.3687$, and for Run 20 the optimized parameters are $K_1 = 0.6430 \times 10^{-2}$ and $K_2 = 0.4132 \times 10^{-1}$.

Table 3 shows two sets of parameters, an optimal set (#1) and a suboptimal set(#2). While there is significant difference in parameter values between these two, they admit similar ASSq values.

| | | | | ASSq | ISSq | |
|---|---|---|---|---|---|---|
| # | $S_0$ | $S_{age}$ | $\sigma_{dp}$ | | Best | Worst |
| 1 | 0.2095 | 399.5 | 7.070 | 0.1349 | 0.1318 | 0.1405 |
| 2 | 0.2417 | 620.2 | 1.191 | 0.1507 | 0.1489 | 0.1567 |

Table 3: Run 20: ASSq for the optimal and suboptimal sets of parameters, and the ISSq for the best and worst samples.

### *5.3. Comparison of The BO and KS models*

#### *5.3.1. Run 23*

Figure 7b presents the dataset along with the mean, best, and worst samples of BO model while figure 7a shows the data and the KS model. The BO fouling $R_f$ has the advantage of nonsmoothness and better represents the qualitative behavior of the data, whereas the KS model can at best capture the mean value of $R_f$. As expected, the BO model more accurately characterizes the breakign behavior observed beginning at 10 hours onward.

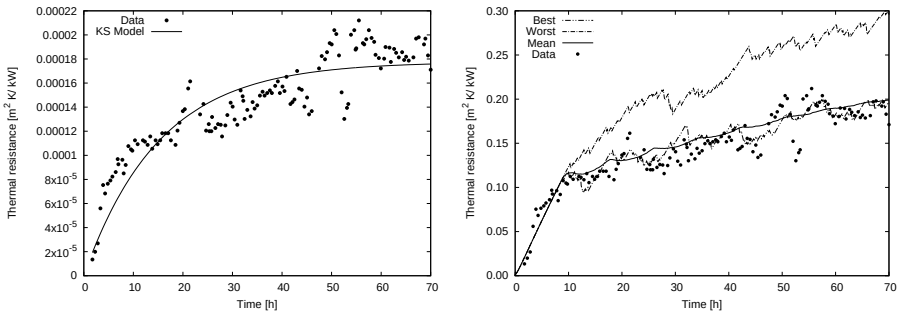


(a) Fitted KS model (b) BO model

Figure 7: Run 23: Comparison between KS model and BO model mean, best and worst samples from 400 samples.

Figure 8 gives probability estimates for the BO model using the optimal parameters, constructing 400 sample models.

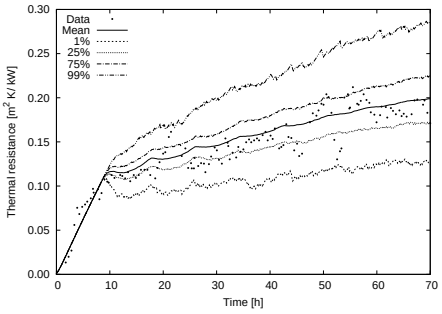


Figure 8: Model mean and percentiles 1%, 25%, 75% and 99%.

In Figure 9 we show $R_f$ values for the best ASSq sample at the beginning, midpoint, and endpoint of the pipe. From these cross-sections, we gain an idea of the break pattern at that location in the pipe.

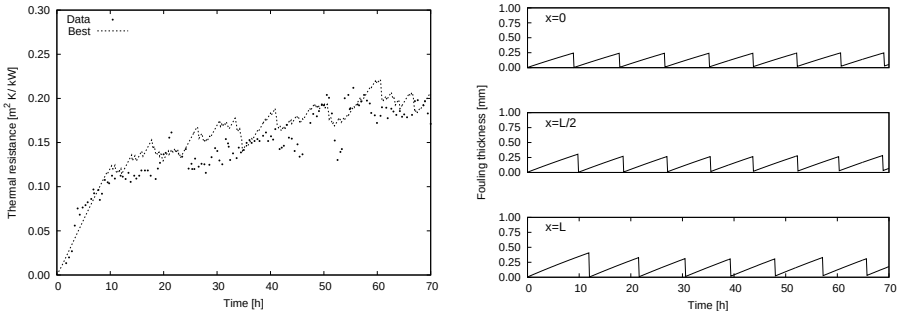


(a) Best sample

(b) Fouling thickness

Figure 9: Run 23: Fouling thickness in the beginning, midpoint, and end of the pipe, using the BO model with parameters from the best ASSq sample.

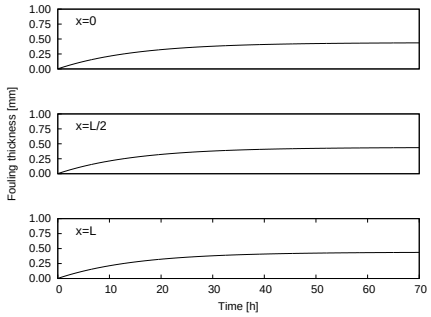


Figure 10: Run 23: Fouling thickness in the beginning, midpoint, and end of the pipe, using the KS model.

Using Akaike differences, we can rigorously compare the fitness of the BO model vs. the KS model. The Akaike difference tries to minimize $\Delta_i$ [27], which is given as $\Delta_i = AIC_i - AIC_{min}$ where $AIC_i$ is the Akaike Information Criterion. Assuming normally distributed errors with a constant variance, the AIC can be written as

$$AIC = n \log(\sigma^2) + 2k_i, \tag{36}$$

where $n$ is sample size and $\sigma^2$ is the residual sum of squares:

$$\sigma^2 = \frac{1}{n} \sum \left( R_{f,j}(t_i) - x_i \right)^2, \tag{37}$$

where $k_i$ is the number of model parameters including $\sigma^2$. The minimal $\Delta_i$ value is assigned by definition $\Delta_i \equiv \Delta_{min} \equiv 0$.

Table 4 shows the ASSq measure and the Akaike differences for both models for Run 23. By both measures, the BO model is preferable over KS.

| | BO | KS |
|---|---|---|
| ASSq | 0.0913 | 0.1267 |
| AIC | -0.2909E+04 | -0.2320E+04 |
| $\Delta_i$ | 0.0 | 588.62 |

Table 4: Run 23: Model selection criterions.

### 5.3.2. Run 20

Figure 11a shows together the data the best, worst samples and the mean for the optimal choice of parameters #1 under the BO model. Figure 11b shows analogous results for the suboptimal parameter set #2. We observe a substantial differnce in qualitative behavior between the models generated by these two sets of parameters. It is important to note, however, that the overall fouling thickness in this case is about 4 times smaller than that of Run 23, so the relative difference is comparatively smaller. Fig 12 displays the calibrated KS model.

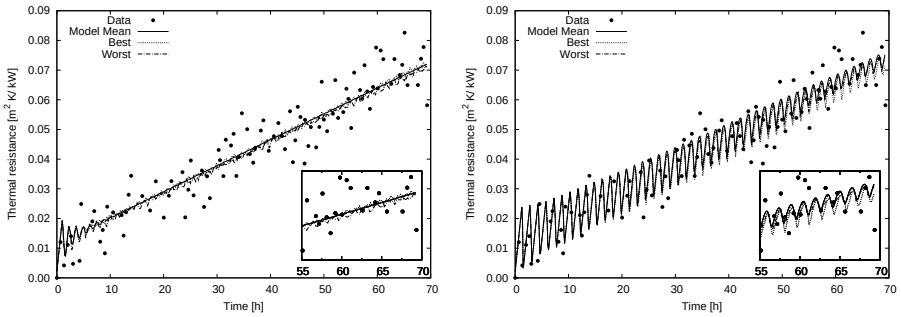


(a) Optimal set (b) Suboptimal set

Figure 11: Run 20: BO models, mean, best and worst samples

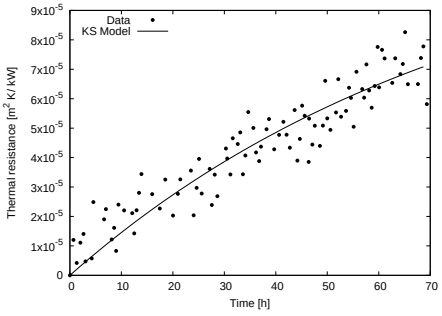


Figure 12: Run 20: KS model.

Figure 13 shows the percentiles for values predicted under the BO model

for the optimal and suboptimal parameter sets, with a sample size $n = 400$. In contrast to the Run 23 models, the models predicted for Run 20 vary less in their qualitative behaviors over the 400 samples.

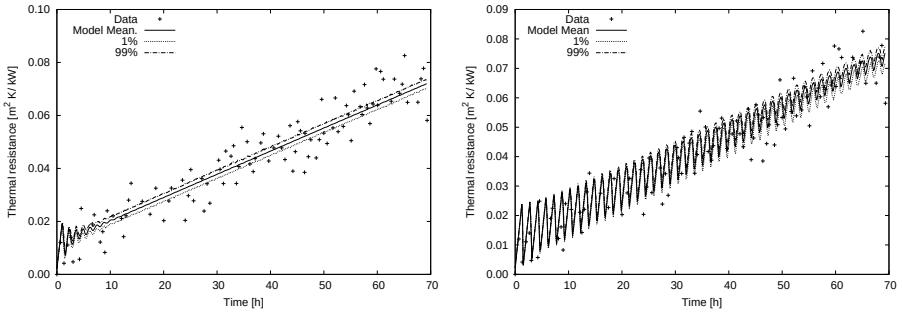


(a) Optimal set (b) Suboptimal set

Figure 13: Run 20 - BO models, mean and percentiles 1% and 99%.

Figure 14 shows the thickness of the fouling layer at the beginning, midpoint, and endpoint of the pipe for the optimal BO model, suboptimal BO model, and KS model. While the two sets of parameters for the BO model admit different overall behavior, we see that the frequency of breaks is similar between the two models, and in both models they occur more frequently than what we observed in the Run 23 model calibration.

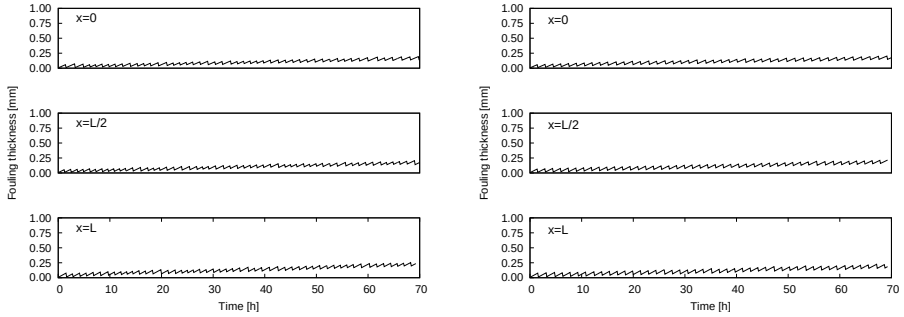


(a) Optimal set

(b) Suboptimal set

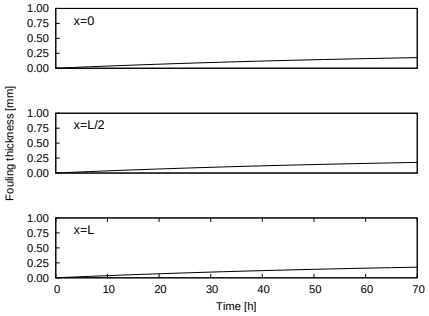


(c) KS model

Figure 14: Fouling thickness in the beginning, midpoint, and end of the pipe.

Table 5 shows the ASSq measure and the Akaike differences for the optimal and suboptimal BO models along with the KO model, calibrated for Run 20. In this case, with both criterions we see that for the optimal parameters set (#1) the BO model is preferable in comparison with KS model. However, KS achieves better by both measures than the suboptimal set (#2).

| | BO | | KS |
|---|---|---|---|
| | #1 | #2 | |
| ASSq | 0.1349 | 0.1507 | 0.1474 |
| AIC | -0,2284E+04 | -0,1899E+04 | -0,1905E+04 |
| $\Delta_i$ | 0.0 | 385 | 379 |

Table 5: Run 20: Model selection criterions.

## 6. Conclusions

One of the distinguishing problems in modeling fouling in heat exchangers is bthe wide range of possible sizes of the pieces that break away from the fouling layer. By taking into account more detailed evaluations of the thermal stress, and accounting for the evolution of material properties of each fouling layer in addition to their temperature, we construct a new model for $CaCO_3$ fouling that better captures the qualitative behavior of the thermal efficiency of heat exchangers, especialy for systems in which larger breaks occur. Our model is able to represent variations in material properties due to time, age, and particular location within the pipe. This gives the BO model the capacity to represent the sawtooth behavior mentioned by Kearn and Seaton in their original paper, and corroborates with observations from experimental and industrial data.

## Acknowledgement

This research is partially supported by the Brazilian Government, through the CAPES (Coordenação de Aperfeiçoamento de Pessoal de Nível Superior), under grants number 2524-14-7 ICES

[1] H. Müller-Steinhagen, Heat transfer fouling: 50 years after the Kern and Seaton model, Heat Transfer Engineering 32 (1) (2011) 1–13.

[2] G. Nellis, S. Klein, The Heat Transfer, Cambridge University Press, 2009, ch 8.

[3] G. F. Hewitt (Ed.), Heat Exchanger Design Handbook, Part 3 - Thermal and Hydarulic Design of Heat Exchangers (Sec. 2.5.1), Begell House Inc, 1998.

[4] R. K. Shah, D. P. Sekulić, Fundamentals of heat exchanger design, John Wiley & Sons, 2003.

[5] T. R. Bott, Fouling of Heat Exchangers, Elsevier Science & Technology Books, 1995.

[6] N. Epstein, Thinking about heat transfer fouling: A $5 \times 5$ matrix, Heat Transfer Engineering 4 (1) (1983) 43–56.

[7] W. L. Mccabe, C. S. Robinson, Evaporator scale formation, Industrial & Engineering Chemistry 16 (5) (1924) 478–479.

[8] R. Sheikholeslami, Tube material and augmented surface effects in heat exchanger scaling, Master's thesis, The University of British Columbia (1984).

[9] D. Q. Kern, R. E. Seaton, A theoretical analysis of thermal surface fouling, British Chemical Engineering 4 (5) (1959) 258–262.

[10] L. F. Melo, T. R. Bott, C. A. Bernardo (Eds.), Fouling science and technology, no. 145 in NATO ASI series, Kluwer Academic Publishers, 1988.

[11] S. G. Yiantsios, A. J. Karabelas, Fouling of tube surfaces: Modeling of removal kinetics, AIChE Journal 40 (11) (1994) 1804–1813.

[12] F. Brahim, W. Augustin, M. Bohnet, Numerical simulation of the fouling process, International Journal of Thermal Sciences 42 (3) (2003) 323 – 334.

[13] M. W. Bohnet, Fouling of heat transfer surfaces, Chemical Engineering Tecnology 10 (1987) 113–125.

[14] S. H. Najibi, H. Muller-Steinhagen, M. Jamialahmadi, Calcium carbonate scale formation during subcooled flow boiling, Journal of Heat Transfer 119 (4) (1997) 767–775.

[15] E. Nebot, J. Casanueva, T. Casanueva, D. Sales, Model for fouling deposition on power plant steam condensers cooled with seawater: Effect of water velocity and tube material, International Journal of Heat and Mass Transfer 50 (1718) (2007) 3351 – 3358.

[16] W. M. Rohsenow, J. P. Hartnett, Y. I. Cho (Eds.), Handbook of Heat Transfer, third edition Edition, McGraw Hill, 1998.

[17] H. Müller-Steinhagen, Cooling water fouling in heat exchangers, in: Advances in Heat Transfer, Vol. 33, Academic Press, 1999, pp. 415–496.

[18] J. R. Cooper (Ed.), Revised Release on the IAPWS Industrial Formulation 1997 for the Thermodynamic Properties of Water and Steam, The International Association for the Properties of Water and Steam, 2007.

[19] L. N. Plummer, E. Busenberg, The solubilities of calcite, aragonite and vaterite in $CO_2 - H_2O$ solutions between 0 and 90°C, and an evaluation of the aqueous model for the system $CaCO_3 - CO_2$-$H_2O$, Geochimica et Cosmochimica Acta 46 (6) (1982) 1011 – 1040.

[20] R. Sheikholeslami, A. P. Watkinson, Scaling of plain and externally finned heat exchanger tubes, Journal of Heat Transfer 108 (1) (1986) 147–152.

[21] D. I. Wilson, E. M. Ishiyama, W. R. Paterson, A. P. Watkinson, Ageing: looking back and looking forward, in: Proceedings of the International Conference on Heat Exchanger Fouling and Cleaning VIII-2009, Schladming, Austria, 2009.

[22] M. W. Bohent, Crystallization fouling on heat transfer surfaces–25 years research in Braunschweig, in: H. Müller-Steinhagen, M. R. Malayeri, A. P. Watkinson (Eds.), Proceedings of the 6th International Conference on Heat

Exchanger Fouling and Cleanings Challenges and Opportunities, 2005, pp. 295–302.

[23] V. Höfling, W. Augustin, M. Bohnet, Crystallization fouling of the aqueous two-component system caso 4/caco 3, in: Proceedings of Heat Exchanger Fouling and Cleaning: Fundamentals and Applications, 2003, pp. 45–52.

[24] C. Carteret, A. Dandeu, S. Moussaoui, H. Muhr, B. Humbert, E. Plasari, Polymorphism studied by lattice phonon raman spectroscopy and statistical mixture analysis method. application to calcium carbonate polymorphs during batch crystallization, Crystal Growth and Design 9 (2) (2008) 807–812.

[25] E. Hairer, S. P. Nørsett, G. Wanner, Solving ordinary differential equations I, Springer-Verlag, 1987, Ch. II-5.

[26] A. Saltelli, M. Ratto, T. Andres, F. Campolongo, J. Cariboni, D. Gatelli, M. Saisana, S. Tarantola, Global Sensitivity Analysis: The Primer, Wiley-Interscience, 2008.

[27] K. Burnham, D. Anderson, Model Selection and Multimodel Inference: A Practical Information-Theoretic Approach, second edition Edition, Springer New York, 2003.

## Appendix A. Fixed Parameters for Run 20 and Run 23 Model Calibration

| Parameter | Run 20 | Run 23 |
|---|---|---|
| $t_1$ | 27.921 | 25.18 |
| $u_0$ | 0.695 | 0.503 |
| dt | 0.125 | 0.125 |
| $k_a$ | 12.0 | 12.0 |
| $k_b$ | 0.001 | 0.001 |
| $k_{a,f}$ | 2.48 | 2.48 |
| $k_{b,f}$ | -0.006 | -0.006 |
| $\epsilon$ | 2.0 $10^{-5}$ | 2.0 $10^{-5}$ |
| $E$ | 122150 | 122150 |
| $\nu$ | 0.29 | 0.29 |
| $K_{r0}$ | 9.80E+11 | 9.80E+11 |
| $\rho_f$ | 2700 | 2700 |
| $\alpha$ | 1.930E-06 | 1.930E-06 |
| $E_y$ | 68.0E+03 | 48.0E+03 |

Table A.1: Parameters for model calibration